Reversible Sliding Motion by Hole-Injection in Ammonium-Linked Ferrocene, Electronically Decoupled from Noble Metal Substrate by Crown-Ether Template Layer

Fumi Nishino[1], Peter Krüger[1,2], Chi-Hsien Wang[3], Ryohei Nemoto[1], Yu-Hsin Chang[3], Takuya Hosokai[4], Yuri Hasegawa[5], Keisuke Fukutani[5], Satoshi Kera[5], Masaki Horie[3*] and Toyo Kazu Yamada[1,2*+]

1. Department of Materials Science, Chiba University, 1-33 Yayoi-Cho, Inage-Ku, Chiba 263-8522, Japan.

2. Molecular Chirality Research Centre, Chiba University, 1-33 Yayoi-cho, Inage-Ku, Chiba 263-8522, Japan.

3. Department of Chemical Engineering, National Tsing Hua University, 101, Sec. 2, Kuang-Fu Road, Hsinchu, 30013, Taiwan

4. National Institute of Advanced Industrial Science and Technology, National Metrology Institute of Japan, Tsukuba Central 5, 1-1-1, Higashi, Tsukuba, Ibaraki 305-8565, Japan

5. Institute for Molecular Science, Myodaiji, Okazaki 444-8585 Japan

Author Information,

Corresponding Author: Toyo Kazu Yamada *E-mail: **toyoyamada@faculty.chiba-u.jp**

Corresponding Author: Masaki Horie *E-mail: **mhorie@mx.nthu.edu.tw**

Version 2024.10.25

Abstract

Artificial molecular machines, especially when based on wheel-and-axle complexes, can generate mechanical motions in response to external stimuli. Ferrocene (Fc) is a key component, but it decomposes at 300 K on metal surfaces. Here, a novel method is presented to construct and control the molecular complex composed of ammonium-linked ferrocene (Fc-amm) and tetrabrominated crown ether (BrCR) on a Cu(111) surface. Fc-amm molecules are periodically arranged on a BrCR monolayer film and imaged using scanning tunneling microscopy and spectroscopy. A lateral motion of the Fc groups by about 0.1 nm is observed for pairs of "edge-on" Fc-amm molecules upon hole injection. This sliding motion is reversible and controlled by the applied voltage. Theoretical analysis indicates that the motion is caused by increased Coulomb repulsion of the hole-doped Fc-amm+ ions and accompanied by a weakening of CH-π interactions. These findings open new avenues for developing nanomolecular devices using on-surface bottom-up processes.

1. Introduction

Artificial molecular devices or motors [1–4], grounded in a "wheel-and-axle" host-guest complex [5–11], can undergo translational and rotational motions in response to external stimuli. These minute motions have yielded substantial advancements in robotic molecular apparatus. Metallocenes, categorized as organometallic sandwich compounds comprising two cyclopentadienyl anion (Cp: $C_5H_5^-$) rings tethered through a metal ion (Cp-M-Cp), intricately interconnect with the central ring inside crown ether (CR) molecules [12–15], engendering the wheel-and-axle: rotaxane complex. Within the metallocene family, ferrocene (Fc: Cp-Fe-Cp) [16], featuring a Fe ion positioned between two Cp rings, manifests internal rotation of the Cp rings along the Cp-Fe-Cp axis (referred to as eclipsed or staggered forms [17]), activated by the redox reaction between Fe^{2+} and Fe^{3+} [18]. This phenomenon results in a mechanically adaptable interface in Fc-based single-molecule junction [19,20]. Additionally, the bulk Fc-CR crystal exhibits millimeter-scale repetitive extension and retraction [8–11], suggesting the potential of such a clathrate compound as a promising foundational element for molecular machinery [21].

Numerous experimental validations have been reported utilizing metallocene-based molecular junctions [22–26], fabricated through the conventional drop-casting metallocene aqueous solutions onto the electrodes. Nonetheless, the feasibility of a bottom-up process for assembling the wheel-and-axle on atomically flat noble metal substrates, a critical determinant for advancing nanomolecular machine devices, remains unclear. The challenge in executing the bottom-up process stems from fundamental surface investigations revealing the decomposition, desorption, or fragmentation of Fc molecules when directly adsorbed onto noble metal surfaces at 300 K [27–32], even under ultrahigh vacuum (UHV) conditions (Fig. 1a).

Extensive experimental findings have elucidated diverse Fc adsorption processes on noble metal substrates: Au [30,33], Ag [27–29,34], Cu [17,28,35], and graphite [32] or Mo surfaces [31]. These observations underscore that Fc alignment, decomposition, and desorption strongly hinge on substrate crystallinity and electronic interactions. Photoemission spectroscopy (PES) and electron energy loss spectroscopy (EELS) experiments have identified Fc adsorption with the Cp-Fe-Cp axis positioned out-of-plane to the surface (face-on) on Ag(100). Conversely, the axis assumes an in-plane orientation (edge-on) on Cu(100) [28,29]. Additionally, it has been reported that Fc desorption from the Ag surface occurs above

250 K in UHV, with potential decomposition due to light illumination during PES measurements [27]. Moreover, partial dissociation during Fc adsorption on Au(111) at 80 K yields a bilayer structure [30]. Although the attachment of side chains to Fc has been identified as a means to curtail decomposition on noble metal surfaces at 300 K [17], thermal diffusion at 300 K results in two-dimensional (2D) self-assembled monolayer (SAM) crystal films (Fig. 1a). Another attempt to stabilize Fc on Ag(111) was demonstrated by utilizing one-dimensional (1D) polyferrocenylene, synthesized by connecting edge-on diiodo-biferrocene single molecules [34]. Thus far, a definitive method for anchoring isolated Fc molecules on a surface at 300 K without decomposition remains elusive.

In this study, we have realized a densely packed 2D ammonium-linked ferrocene (Fc-amm) complex (see Fig. 1a) on top of a well-ordered monolayer of Br_4-dibenzo crown ether (BrCR). The latter can act as a sub-nanometer buffer layer to decouple the electronic interaction between an adsorbed molecular film from the metal substrate, as we have shown previously[13–15]. Upon scanning tunneling spectroscopy (STS) with bias voltage below and above -1.3 V, a reversible switching in the dI/dV map of the "edge-on" adsorbed Fc-amm conformation is observed (Fig. 1b). As the switching voltage (-1.3 V) corresponds to the highest occupied molecular orbital (HOMO) of the Fc group, the changes in the dI/dV map can be identified as a lateral motion of the Fc group by approximately 0.1 nm. We note that for all other ions, including the face-on Fc-amm molecules, no positional changes are detected.

Importantly, the Fc molecular motion is controlled by the sample bias voltage. For a voltage less than -1.3 V, the edge-on Fc-amm molecules are in their electronic ground state. When the bias voltage exceeds -1.3 V, a hole is injected into the HOMO from the STM tip. The hole injection enhances further ionization of Fc-amm, facilitating the well-known redox reaction between Fe^{2+} and Fe^{3+}. Our density functional theory (DFT) calculations show that the edge-on conformation is the most stable adsorption geometry of the Fc-amm molecule on the BrCR/Cu substrate. The ammonium group forms several hydrogen bonds with the crown ring resembling a host-guest reaction in solution. When the Fc group is laterally shifted by ±0.1 nm away from the equilibrium, the ammonium group remains attached to the crown by hydrogen bonds. Such a 0.1 nm shift raises the potential energy by about 0.1 eV. We show that this cost in adsorption energy can be overcome by a gain in electrostatic energy for a pair of nearest neighbor ferrocene units where one carries an extra charge of $+e$. This suggests that

the observed reversible molecular shift is caused by the increased Coulomb repulsion between neighboring Fc-amm$^+$ cations upon hole injection into the HOMO.

Our findings provide insights for the development of Fc-based molecular junctions: (1) we demonstrated how to grow an ordered 2D Fc-amm array on an atomically flat noble metal Cu(111) surface without decomposition, even at ambient temperature by utilizing the trapping and protecting functionalities of the crown ether; (2) only the edge-on Fc-amm can be utilized for the molecular sliding junction; and (3) the lateral motion can be controlled simply by applying a bias voltage.

2. Methods and Materials

2.1 Home-built low-temperature UHV STM setup.

STM measurements were performed using home-built UHV-STM equipment consisting of STM, preparation, and deposition chambers. The base pressures of each chamber were below 5.0×10^{-8} Pa, 2.0×10^{-8} Pa, and 1.0×10^{-7} Pa, respectively [13,14,36,37]. Samples and STM tips were transferred between chambers using transfer rods without breaking the UHV. Gate valves separated each chamber. A UHV cryostat (CryoVAC) in the STM chamber was used to cool down the STM setup. We used sharp tungsten tips as STM probe tips utilizing both conventional chemical etching and flame etching, producing a sharp tip within 3 seconds [38–41]. The Cu(111) was cleaned in the preparation chamber [36,37,42,43], and BrCR molecules were deposited in the deposition chamber with a single-molecule-level control utilizing quartz crystal microbalance (QCM) [44].

2.2 STM / STS measurements.

A home-built STM combined with the Nanonis SPM controller BP4 obtained topographic images of sample surfaces in a constant current mode since the tunneling current (I) detected by the tip is exponentially proportional to the tip−sample separation (z) via $exp(- (8\, m\, (\Phi \pm eV/2))^{1/2}\, z/\hbar)$, where m: electron mass, $\hbar$: Planck constant, Φ: apparent barrier height between tip and sample, and V: set point sample bias voltage [45,46], we can measure the surface corrugations in the order of 1 pm.

STS measures sample surface local density of states (LDOS) [45,46]. I, as a function of sample bias voltages (typically, from −2 V to +2 V), was measured under feedback off condition (one single curve was measured within 50−200 ms) by fixing the tip−sample separation ($z = z_c$), which was determined by the setpoint voltage (V_s) and the current (I_s). The obtained $I(V)$ curves were numerically differentiated, and differential conductance (dI/dV) curves were obtained: $dI/dV \sim \rho_s\, (- (8\, m\, (\Phi \pm eV/2))^{1/2}\, z/\hbar)$. The STM/STS data were analyzed using WSxM 5.0 Develop 10.2 software and Gwyddion 2.53 [47].

2.3 XPS measurements.

XPS measurements were conducted on the home-built UHV apparatus equipped with a hemispherical electron energy analyzer (MBS A-1) (Supplementary Note, Figs. S11 and S12, and Table S2). All XPS measurements were performed at 300 K with an excitation energy of MgK_{α} line 1253.6 eV. All spectra were processed as the binding energies are respective to the Fermi edge of the Au polycrystal. The Fe 2*p* spectra are fitted with a Doniach-Sanjic line shape.

2.4 Cu(111) and Au(111) cleaning process.

We used Cu(111) and Au(111) single crystals (diameter 6 mm, MatecK, 99.999%). It was carefully sputtered (Ar^+, +1.0 keV, 400 nA) and annealed (~820 K) in the preparation chamber ($<5.0\times10^{-8}$ Pa) to obtain clean and atomically flat surfaces (Supplementary Fig. S2).

2.5 Molecular evaporation in UHV.

BrCR and Fc-amm molecules were deposited in the deposition chamber ($<3.0 \times 10^{-7}$ Pa) (Supplementary Fig. S3). To control precisely the amounts of deposited molecules on the substrates at 300 K, we used the quartz crystal microbalance (QCM) [44]. The same parameters (z-ratio = 1, density = 1) were taken to operate QCM and set QCM at the same distance from the crucible (110 mm). A flowing current radiatively heated the quarts crucible through a tungsten wire filament (diameter 0.3 mm). The crucible temperature was monitored using the alumel-chromel thermocouple, which contacted the bottom of the crucible. Fc-amm deposition rate of 0.026 nm/min was used at the crucible temperature of 348 K (1×10^{-5} Pa). BrCR deposition rate of 0.140 nm/min was used at the crucible temperature of 383 K (2×10^{-8} Pa).

2.6 Molecules and Characterization.

Synthesis and characterization of 4,4',5,5'-tetrabromodibenzo[18]crown-6 ether (BrCR) and $[ferrocenylmethyl(methyl)ammonium]^+(PF_6)^-$ (Fc-amm) was performed based on the method described in the literature [5,11]. JEOL JMS-T200GC AccuTOF GCx observed field-desorption mass spectra (FDMS) of sublimates. Single-crystal X-ray crystallography for the crystals of the complex of

BrCR and Fc-amm was performed using the Rigaku XtaLAB Synergy-DW system and Bruker Single Crystal D8 Venture diffractometer (Supplementary Table S1). CCDC 2326995 contains supplementary crystallographic data for new crystals in this article. These data can be obtained free of charge via www.ccdc.cam.ac.uk/data_request/cif.

2.7 DFT calculation method.

DFT calculations were performed (Supplementary Fig. S14) with the PBE exchange-correlation potential and the DFT-D3 dispersion corrections [48], using the projector-augmented-wave code VASP [49,50]. The theoretical lattice constant of fcc Cu is 0.35686 nm, which is in good agreement (-1%) with the experiment. The Cu substrate was modeled with two monolayers of Cu(111) in a 7×4 supercell, which corresponds to the experimentally observed periodicity of BrCR/Cu [13]. The plane-wave energy cut-off was set to 400 eV, and a 2×4×1 Monkhorst-Pack *k*-point mesh was used. The vacuum layer between repeated slabs was at least 1.2 nm. The atomic positions of the lowest Cu monolayer were fixed. The coordinates of all other atoms were fully optimized until the forces were less than 0.1 eV/nm. The Fc-amm molecule was put on the BrCR/Cu substrate starting from various adsorption positions in different orientations to find stable structures. The present computational settings are similar to our previous BrCR/Cu studies [13,14]. However, the DFT-D3 scheme is used here instead of the previously rescaled DFT-D2 for the dispersion forces. Also, the Cu substrate is modeled with a thinner slab because the Fc-amm molecule interacts indirectly with the Cu substrate through the BrCR film. Neither modification affected the results on BrCR/Cu in any significant way.

3. Results and Discussion

3.1 STM imaging of isolated Fc-amm molecules

Given that the decomposition of Cp-Fe-Cp may transpire when the interaction between the Cp ring and the noble metal substrate disrupts the Fe-Cp bonding, the electronic decoupling between Fc and the conductive substrate can fortify the integrity of the Fe-Cp bonding (Fig. 1a). However, this electronic decoupling can result in an extremely weak interaction with the substrate, fostering increased thermal diffusion of the adsorbed Fc on the surface, culminating in the formation of a 2D SAM film. This implies that achieving a single Fc molecule junction necessitates a substrate endowed with electronic decoupling and trapping functionalities (Fig. 1a), a pivotal requirement for realizing a metallocene-based single molecular junction at 300 K.

In the context of this inquiry, guest Fc-amm molecules were adsorbed onto the host BrCR SAM nanoporous film at 300 K in UHV. This choice was guided by the well-established host-guest supramolecular network in the bulk system using BrCR and Fc-amm [5,11,51].

The molecular structures of the Fc-amm guest and BrCR host complexes within the bulk crystal were elucidated using single-crystal X-ray crystallography (Fig. 1c, Supplementary Fig. S13, Table S1, and CCDC: 2326995). An intriguing observation arises within the Fc-amm/BrCR single crystal bulk: the alignment of the Cp-Fe-Cp axis is not unidirectional, as both face-on and edge-on configurations of the Fc-group coexist within the unit cell. This phenomenon is upheld by a consistent CH-π interaction distance of 0.30 nm in the edge-on Fc-group configuration and a π-π interaction distance of 0.43 nm in the face-on configuration. The total molecular heights for the Fc-group and the catechol moiety in these configurations were estimated to be 0.80 nm for edge-on and 0.88 nm for face-on, based on space-filling models of the bulk crystal.

Molecular morphology and electronic structures were scrutinized utilizing a home-built scanning tunneling microscopy and spectroscopy (STM/STS) setup operated at cryogenic temperatures in UHV (Fig. 1b) [14,36,37].

The atomically flat Cu(111) as the substrate (Supplementary, Fig. S2) was utilized since BrCR forms an ordered (7 × 4) 2D-SAM array on Cu(111) (Supplementary, Fig. S4), with two benzene rings of

each BrCR contacting parallel to the surface. This arrangement results in the O-C-O ring assuming a flat structure [13,14,52], thereby creating the 2D nanoporous array.

Fc-amm molecules were adsorbed on this BrCR array in UHV at 300 K (Supplementary, Fig. S3), and STM at the cryogenic temperature resolved the adsorption configuration. Figure 1d presents an STM topographic image conducted on the BrCR-ordered nanopores after the deposition of 0.1 monolayers (MLs) of Fc-amm. The adsorbed Fc-amm single molecules were trapped on the BrCR array prepared on Cu(111), which is an exceptional case since all Fc-amm molecules adsorbed on the BrCR array on Au(111) widely used as device electrodes thermally diffuse and traverse the BrCR descending steps due to a bending structure of BrCR ring, as similar to the bulk phase in Fig. 1c [53–55], fostering weak interaction between Au and BrCR, thereby lacking trapping ability, and eventually forming Fc-amm islands on the Au(111) terraces (Supplementary, Figs. S7-S9). This experimental evidence in Fig. 1d proves the trapping functionality of the BrCR array on Cu(111).

The regularity of the Fc-amm single-molecule suggests that adsorbed Fc-amm compounds are likely to possess uniform structures on the BrCR array rather than forming a disordered arrangement akin to the direct adsorption of Fc-amm on Cu(111), resulting in a disordered monolayer film, as illustrated in Supplementary, Fig. S5. This confirms that the BrCR array exhibits a protective function, preventing decomposition and disordering. The BrCR array in Fig. 1d comprises alternating slot rows delineated by red and blue parallelogram-shaped slots. The isolated bright dot is adsorbed, spanning two nanopores. The height profile across this dot indicates a width of approximately 1.5 nm, comparable to the size of the Fc-amm/BrCR complex in bulk (Fig. 1c), signifying the presence of an Fc-amm single molecule in the dot.

DFT calculations were performed to find the possible adsorption configurations of Fc-amm molecules on a BrCR monolayer on Cu(111). The most stable conformation and the second most stable one, which is 0.25 eV per molecule higher in energy, are shown in Fig. 1e. Various other conformations have been found as solutions for structural optimization. Still, they are less stable by at least 0.7 eV/molecule (Supplementary, Figs. S14-S16). In both structures in Fig.1e, the Fc part interacts with a benzene ring of BrCR, and the amm-part is above the crown ring, making hydrogen bonds with the oxygen atoms of the crown. This type of arrangement has been anticipated by the XRD analysis of the

Fc-amm/BrCR bulk structure, as seen above and in Supplementary Fig. S13. An essential difference to the bulk is that the BrCR monolayer lies flat on the Cu(111) substrate [13].

The only difference between the structures shown in Fig. 1e is the orientation of the Fc-group. We find that edge-on is more stable than face-on, but the energy difference is relatively small (0.25 eV). Depending on the arrangement of the PF_6^- counter-ions, which have been disregarded here, the face-on configuration may stabilize further, explaining the coexistence of the two orientations in the experiment. Other conformations are less stable (by at least 0.7 eV; see Supplementary, Figs. S14 and S15). This indicates that the most critical host-guest interactions are π-π bonds between the frontier orbitals of the Fc-group and BrCR benzene ring and hydrogen bonds between the amm-group and the BrCR crown; see Supplementary for details. We note that the structure of the BrCR monolayer hardly changes upon Fc-amm adsorption. This demonstrates that the BrCR/Cu(111) template structure is very stable, in agreement with the experiment, and indicates that the BrCR molecules interact much more strongly with the Cu substrate than with the guest molecule Fc-amm.

The apparent height in STM topographic images highly depends on the tunneling pathway from the STM tip to the Cu substrate. When the STM tip is positioned over a BrCR molecule, electrons tunnel directly through the BrCR molecule. However, when the tip is positioned over an Fc-amm molecule, electrons must pass through both the Fc-amm and BrCR molecules. This results in lower conductance compared to tunneling, which occurs only through the BrCR molecule. Consequently, this difference in electronic properties between the Fc-amm and BrCR molecules significantly alters the apparent height in STM images. The tip position over the BrCR surface is much higher than that of the Fc-amm molecules. This effect is well-known for organic molecules on insulating substrates. [56] The apparent height of approximately 200 pm for the Fc-amm molecules on BrCR, which is much lower than the DFT-simulated height of approximately 400 pm, further supports the notion that the subsurface BrCR layer functions as an insulating layer, effectively serving as an electronic decoupling layer.

3.2 Fc-amm regularity trapped on BrCR array

Although the isolated Fc-amm molecules were observed on the BrCR (Fig. 1d) because the BrCR captures the guest Fc-amm molecule, it is rare. The probability of trapping could be diminished on the

terrace. The STM topographic image in Fig. 2a shows the surroundings of the isolated Fc-amm molecule. It is discernible that the central region of the BrCR islands remains exposed (low density), whereas other Fc-amm molecules configure one-dimensional connections proximate to the step edges. This observation signifies the thermal diffusion of adsorbed Fc-amm molecules at 300 K on the BrCR/Cu(111). A plausible scenario unfolds since Fc-amm molecules envelop all BrCR island step edges. Initially, adsorbed Fc-amm single molecules thermally diffuse on the BrCR surface until they reach the edges of the descending step. Subsequently, they are trapped until all edges are coated by Fc-amm molecules, as depicted in Fig. 2a. Once the edges are fully covered, additional Fc-amm molecules can persist on the BrCR island, culminating in the formation of the connections through intermolecular interactions.

Figure 2c presents a magnified image of the BrCR nanoporous array following the deposition of 0.1 MLs of Fc-amm. Here, BrCR formed an ordered array with unit cell vectors of $\boldsymbol{a_1}$ = 0.9 nm, $\boldsymbol{a_2}$ = 1.7 nm, θ = 89°, aligning with previously reported values of $\boldsymbol{a_1}$ = 0.90 nm, $\boldsymbol{a_2}$ = 1.74 nm, θ = 88.9° [13,14,52].

As we primarily observed two types of bright dots on the BrCR array, α and β, the dimensions of individual dots align with the Fc-amm/BrCR complex (Fig. 2c) and the BrCR nanopore size, approximately 1 nm. The α molecule, represented by one bright dot with a stick extending from the right-hand side, constitutes the smallest unit on this surface, consistently positioned at the BrCR nanopore location (cross marks in Fig. 2c). Specifically, the bright spot aligns with the nanopore center. Given the CR ring's preferential capture of the Fc-amm ligand in the bulk complex (see Fig. 1c), the bright spot in the α molecule is presumed to be the side ligand, with the extending stick identified as the Fc.

In contrast to the bulk scenario, the BrCR array on Cu(111) presents two types of nanopores, CR-slot and Br-slot (lower panel in Fig. 2b), which are experimentally challenging to distinguish. However, adjacent slots can be classified as either red or blue slots. Each forms a row parallel to the unit vector of $\boldsymbol{a_1}$. The red and blue slot rows alternate with reflection symmetry. The model in the right panel in Fig. 2c illustrates how experimentally observed Fc-amm molecules are positioned on the BrCR nanopore rows. Here, the α molecules are trapped by the red slots.

Notably, the neighboring molecule of the α molecule, named the α' molecule and trapped by the blue slot, undergoes a rotation of about 90 degrees following the subsurface slot direction (Fig. 2c). It exhibits the same size and shape, but α' possess the mirror reflection relationship between α respect to BrCR array unit cell vector $\boldsymbol{a_1}$: the stick extends from the left-hand side.

Subsequently, our attention turned towards the β molecule, characterized by a parallelogram shape, positioned within the blue slot flanked by two α molecules. Similar to the relationship between α and α', the β' molecule, which has the same size and parallelogram shape as the β molecule, is mirror-symmetrical with β concerning the unit cell vector $\boldsymbol{a_1}$. These were similarly observed at the red slot surrounded by two α' molecules. Since both β and β' exhibit approximately twice the size of α, spanning two slots, they could conceivably consist of two Fc-amm molecules.

Depending on how the Fc-amm side ligand contacts with the Br-slot or the CR-slot, the Cp-Fe-Cp axis would modify and could orient vertically or horizontally, referred to as face-on or edge-on Fc-group. It has been reported that the Fc-groups within the Fc-complexes manifest as bright dots with an off-centered dark, dim spot in STM topographic images when the Cp-Fe-Cp axis is oriented vertically to the surface (face-on Fc-group). Hence, the observation in the STM image of Fig. 2c, which does not show such dark, dim spots, could imply that the discrete Fc-amm entities within the one-dimensional connections consist of Fc-amm complexes with the edge-on orientation, as predicted by the theoretical calculations in Fig. 1e.

We conducted a tally of α, α', β, and β' molecules, culminating in their statistical distribution. This analysis revealed the energetically stable adsorption configurations on the BrCR nanopores: α = 34%, α' = 38%, β = 11%, and β' = 17%. Next, we determined the ratio of Fc-amm molecules within these complexes by counting β and β', each of which includes two Fc-amm molecules: α = 27%, α' = 30%, β = 17%, and β' = 26%. No significant variance was observed, indicating that these four adsorption sites could be energetically equivalent.

This experimental evidence of the equivalent ratio between the mirror reflection relationship between α and α', as well as β and β,' further supports the adsorption of the Fc-amm molecules on BrCR/Cu(111) could be edge-on since the equivalent molecular orientation concerning the substrate before and after the molecular inversion is only possible for the edge-on case. In the face-on case, the Fc-group must flip upside down, which should not be the same observation in the image.

Furthermore, it is noteworthy that the isolated Fc-amm molecules adsorbed according to a rule, resulting in the geometric connection: a recurring sequence of α-β-α and α'-β'-α'. The table in Fig. 2b summarizes the connection rules derived from the experiments. Rule (1) dictates that α complexes can connect with α' and β, but not with α and β.' Rule (2) asserts that α' complexes can connect with α and β' but not with α’ and β. Rule (3) posits that β and β' complexes can connect with α and α', respectively. Due to the electronic decoupling functionality of the BrCR array, cutting electronic interactions from the Cu substrate, the intermolecular interactions between Fc-amm and subsurface BrCR, and concurrently among Fc-amm molecules, dictate the Fc-amm regularity. The empirical proof that all Fc-amm molecules adsorb to the BrCR nanopore arrangement implies that the intermolecular interaction between Fc-amm and BrCR can trap and dictate the adsorbed Fc-amm direction, aligning with the subsurface slot direction. Nevertheless, this trapping interaction from the BrCR alone cannot orchestrate the geometric α-β-α or α'-β'-α' formation. This intricate arrangement must be attributed to another factor, specifically the intermolecular interaction among Fc-amm.

3.3 Dense-packed Fc-amm array formation

The STM topographic image in Fig. 2d illustrates the evolution of Fc-amm molecules on the BrCR nanopores, correlating with an augmented deposition increasing from 0.1 to 0.3 monolayers (MLs). This delineates a marked phase transition from a one-dimensionally aligned structure comprising isolated Fc-amm molecules to a well-ordered, dense-packed array structure (Supplementary, Fig. S6).

As elucidated in Fig. 2a-c, the behavior of isolated Fc-amm molecules is influenced by the compelling intermolecular interaction between Fc-amm and BrCR and another intermolecular interaction among Fc-amm molecules. In Fig. 2d, the transition to a densely packed, brick-like structure is perceptible near the step edge where Fc-amm molecules are densely arranged. This suggests that the dramatic phase shift is induced by the spatial separation between Fc-amm molecules, where the attractive interaction among Fc-amm molecules surpasses the attractive interaction between Fc-amm molecules and the BrCR.

A pivotal structure change in Fig. 2d is the absence or weakening of the trapping functionality from the BrCR. Multiple domains in the Fc-amm array with unit vectors of $\boldsymbol{b_1}$ = 2.4 nm, $\boldsymbol{b_2}$ = 4.2 nm, θ =

106° were identified (arrows in the right panel in Fig. 2d), which significantly differed from the BrCR unit cell, both in size and angle: $\boldsymbol{a_1}$ = 0.9 nm, $\boldsymbol{a_2}$ = 1.7 nm, θ = 89°.

Specifically, this experimentally observed misalignment indicates a weak interaction between the Fc-amm molecules in the 2D ordered array and the subsurface BrCR. Therefore, the orderliness in the densely packed Fc-amm array is likely governed by the intermolecular interactions between the Fc-amm molecules. We have checked the area and alignment for both Fc-amm and BrCR arrays. The areas of $\boldsymbol{b_1 \cdot b_2}$ and $\boldsymbol{a_1 \cdot a_2}$ have been calculated as 9.7 nm^2 and 1.5 nm^2, respectively, including six Fc-amm molecules and one BrCR molecule within each unit.

Given that the transition from the α-β-α connection to the brick-like structure was also observed in the high-density region near the step edges in the center panel in Fig. 2d, it is plausible to assume that the isolated α-β-α formation was compressed, leading to the formation of the densely packed brick-like structure. This infers that one brick could encompass four Fc-amm molecules, mirroring the α-β-α chain's inclusion of four Fc-amm molecules (Fig. 2c).

3.4 Identifying Fc-group position within Fc-amm array

The Fc-amm array exhibits a distinctive brick-like structure, comprising both larger and smaller bricks, delineated by white boxes in Fig. 3a. A meticulous examination of atomic positions within the Fc-amm array was conducted through STS in UHV at 4.6 K. Figure 3b presents a magnified STM topographic image, wherein dI/dV spectra, indicative of the LDOS for each pixel position, were measured, unveiling the positions of the Fc and the PF positions within the array. The right panel in Fig. 3b shows a concurrently obtained dI/dV map at -2.1 V. The color scale from blue to red in the dI/dV maps signifies higher to lower LDOS.

The experimentally acquired 10,000 dI/dV spectra in Fig. 3b were discerned to primarily fall into three LDOS categories, as illustrated in Fig. 3c: (1) dI/dV spectra obtained on the Fc-amm with the HOMO peak at -1.3 eV, the LUMO peak above +1.0 eV, and a band gap width of about 2.3 eV (depicted by blue and red lines), (2) dI/dV spectra obtained on the Fc-amm with no significant peaks within ±2 eV (a band gap width >4 eV) (depicted by the green line), and (3) dI/dV spectra obtained on the BrCR layer, revealing the HOMO peak at -1.2 eV and the LUMO peak above +1.0 eV (depicted by the grey

line).

The lower panel in Fig. 3c presents the results of DFT theoretical calculations of LDOS in the bulk Fc-amm crystal. Here, the Fc-group exhibits HOMO and LUMO peaks with a band gap width of approximately 2 eV (indicated by the blue line), while the PF_6^- side chain displays no LDOS peaks with a band gap width exceeding 4 eV (indicated by the green line). A comparison between DFT and experimental results in Fig. 3c suggests that the Fc-group could be located at local positions with HOMO/LUMO peaks (represented by blue and red dots in the inset image). The PF_6^- side chain could be found at local positions with no LDOS peaks (depicted by the green dot in the inset image). The complete theoretical LDOS is plotted in Supplementary Fig. S10. Additionally, the experimentally measured HOMO position aligns with the findings in the case of Ferrocene-bridged trisporphyrins on Au(111) [33].

Another aspect from Fig. 3c was that all dI/dV spectra of the adsorbed molecules on Cu(111) have a dI/dV value of 0.0 nA/V near the Fermi energy, indicating a band gap. Therefore, the STM tip could image the substrate Cu(111) through adsorbed molecules by taking the dI/dV map at 0 eV (see the inset in Fig. 3c), where molecules were absent since the electrons from the tip tunneled through the molecular gap into the substrate Cu. This implies that the host BrCR nanopore array could be an electronic decoupling layer from the metallic substrate Cu(111).

Thus, we could discern the Fc-group and PF positions within the 2D array, as indicated by arrows in Fig. 3b. The larger box in Fig. 3a comprises four Fc-amm molecules, while the smaller box includes only two. The former may correspond to the isolated α-β-α formation in Fig. 2, where α and β may consist of one and two Fc-amm molecules, respectively.

Another noteworthy observation from the STM topographic image in Fig. 3b is the off-centered distinctive dark, dim spots, reported as a hallmark of the face-on Fc-group (compare complexes including Fc-groups on Cu(111) and Cu(100) [17], where the five-membered ring lies parallel to the surface). This contrasts the isolated case in Fig. 2, where the Cp-Fe-Cp axis of all Fc molecules could be tilted or have an edge-on position, with the π-plane of the five-membered ring perpendicular to the surface.

However, following the phase transition to the dense-packed Fc-amm array, liberated from the BrCR trapping, the Fc-amm could adopt an energetically stable configuration similar to the bulk crystal. Two of the four Fc-amm molecules inside the larger box and both Fc-amm molecules in the smaller box

could assume the face-on configuration.

The STS results in Fig. 3b reveal that the densely packed Fc-amm array comprises three distinct Fc-amm compounds, denoted as type I, II, and III. In Fig. 3d, the corresponding model of the smaller and larger boxes is presented, wherein the positions of face-on Fc-group, edge-on Fc-group, and the PF side ligands are indicated by blue, red, and green dots, respectively.

Initially, within the larger box (Fig. 3d), the face-on Fc-amm with the PF_n^- ligand (type I) is situated on the upper and lower sides, exhibiting C_2 symmetry (PF_n^- ligand, *n* could be below six, Supplementary Note). Between these, two edge-on Fc-amm molecules are positioned with C_2 symmetry (type II), albeit smaller in size compared to type I. The STS map demonstrates no significant band gap region within type II, suggesting the absence of the PF_n^- ligand. Similarly, within the smaller box, two C_2-symmetric face-on Fc-amm molecules are present (type III), smaller than type I.

We further performed DFT simulations of face-on and edge-on Fc-amm on BrCR/Cu(111) at the HOMO energy level, as depicted in Fig. 3e. The calculated LDOS peaks for Fc-amm in face-on (upper panel) and edge-on (lower panel) orientations are presented. Charge maps, corresponding to the experimentally obtained d*I*/d*V* maps, reveal that charges are localized around the Fe positions within the Fc-amm, suggesting that the higher intensity spots in the d*I*/d*V* maps correspond to the Fe positions. Conversely, the simulated STM topographic images in Fig. 3e (top view) indicate that the C-H bonds of the Cp-ring could be observed, as these are the closest to the STM tip.

We analyzed the variation in LDOS within type I and III Fc-amm molecules (Fig. 3f). The d*I*/d*V* intensity profiles along the four arrows intersecting type I and III Fc-amm molecules (shown in the inset STM images in Fig. 3f) are depicted as a 3D d*I*/d*V* map in Fig. 3f, with the *x*, *y*, and *z*-axes representing distance, energy, and d*I*/d*V* intensity, respectively. This mapping indicates that type I exhibits a sudden change between the Fc-group and the PF_n^- ligand, whereas type III lacks PF_n^- ligand like LDOS, indicating the absence of the PF_n^- ligand.

The STS results illustrated in Fig. 3 suggest the following classifications: type I corresponds to the face-on Fc-amm with the PF_n^- ligand, type II to the face-on Fc-amm without the PF_n^- ligand, and type III to the edge-on Fc-amm without the PF_n^- ligand. Specifically, it is inferred that approximately 67% of adsorbed Fc-amm may undergo loss of the PF_n^- ligand during the deposition process, likely occurring during the heat treatment within the crucible under ultra-high vacuum conditions. Indeed, FDMS (Supplementary, Fig. S1) of the sublimed Fc-amm from bulk crystals indicates the generation

of several Fc-amm compounds with different ligands after heating to temperatures ranging from 403 to 433 K.

To characterize these three varieties of Fc-amm compounds, further X-ray photoelectron spectroscopy (XPS) analyses were conducted at 300 K under UHV conditions. XPS spectra for F 1*s* and Fe 2*p* of Fc-amm/Au(111), Fc-amm/Cu(111), and Fc-amm/BrCR/Cu(111) are juxtaposed (Supplementary Note, Figs. S11 and S12, and Table S2). In contrast to STM, XPS furnishes integrated outcomes from the entire surface. Additionally, light irradiation induces molecular decomposition during the assessment. Considering these two aspects, it is challenging to establish a quantitative correspondence with the results obtained by STM. Nonetheless, XPS findings correlate with our STM observations, indicating that the Fc-group on BrCR remains intact. At the same time, the PF_n^- ligand may undergo decomposition during the thermal sublimation process, aligning with the STM/STS results in Fig. 3. Furthermore, no significant shifts or alterations were discerned for the carbon, nitrogen, and oxygen peaks from the BrCR in the Fc-amm/BrCR/Cu(111) system, signifying the absence of a chemical bond between the BrCR and Fc-amm molecules, thereby illustrating that Fc-amm is physisorbed on the BrCR film.

3.5 Motion activation in Fc-amm array

As corroborated by the STS electronic structure measurements in Fig. 3, the entire Fc-group showcased the HOMO peak at -1.3 eV. To induce motion, hole carriers from the STM tip were introduced into the Fc molecular orbital. Subsequently, we observed substantial variations in STM/STS images below and above the HOMO peak energy.

The STM energy diagram in Fig. 4a illustrates the trajectory of electrons or holes traversing from the tip to the Cu(111) substrate through the double barrier system when applying a bias voltage of -1.3 V to the sample. In this context, the hole from the tip could tunnel into the Fc-group's HOMO peak and traverse to the Cu band via the BrCR HOMO peak. Figure 4b portrays two dI/dV maps acquired at +2.3 V (left panel), far from the HOMO peak, and at -1.3 V (right panel), corresponding to the HOMO peak energy. A comparison of the Fc-group position in both maps suggested a shift in edge-on Fc-group positions (blue circles in the model). In contrast, other face-on Fc-group and PF side chain positions remained unchanged. This shift in edge-on Fc-group positions led to significant variations in the STM topographic images. Figure 4c illustrates one such demonstration: the tip scanned from bottom to top (-1 V to -2 V) in the left and from top to bottom (-1 V to -2 V) in the right panel. The arrangement of bright spots changed; for instance, the line crossing the center two spots shifted from 29 degrees at -1 V to 53 degrees at -2 V, while the 2D array regularity was maintained. These motions were also distinctly observable in the movies (see Supplementary, Movies S1-S3).

A series of STM images depicting the same spatial region under various bias voltages is illustrated in Fig. 4d. The measurement of the two-spot angle was conducted. Its summary is displayed in the graph presented in Fig. 4e. This graphical representation clearly illustrates an approximate variation of 30 degrees occurring below and above the Fc HOMO energy position at -1.3 eV. Additionally, the lateral displacement of the Fc-group position is approximately 0.1 nm.

Figure 5a summarizes the experimentally observed reversible lateral position shifts of Fc-amm on BrCR/Cu(111) by applying a bias of -1.3 V. Only the edge-on Fc-amm moves, while the face-on Fc-amm remains stationary. Figure 5b shows the DFT calculation results. We calculated the total energy variation of the edge-on Fc-amm as a function of the Fc lateral position along the y-axis in Fig. 5b. To this end, we turned the Fc-amm molecule around the N-atom by different angles within ±15 degrees. Then, the structure was reoptimized for each angle with the y-coordinate of the Fe atom fixed, but all

other degrees of freedom fully relaxed. As a result, the amm-group hardly moved but remained attached to the crown ring by several hydrogen bonds. The energy minimum (ΔE = 0 meV) corresponds to the energetically stable edge-on Fc-amm shown in Fig. 1e. From the energy curve, it can be inferred that if an external stimulus with an energy increase of about 100 meV is applied, the Fc-group may shift laterally by about 0.1 nm. Another interesting point is that the DFT results show that the elongation of CH-π interaction between the Cp-ring of Fc-amm and BrCR co-occurs with the lateral position shift (see the right-hand side panel at Δy = +0.1 nm in Fig. 5b).

The lateral shift of the Fc group is observed when holes are injected into the Fc-HOMO at a sample bias voltage V_s < -1.3 V. The HOMO is mostly made of Fe-3*d* states and essentially localized on the Fe atom inside the Fc group, as seen in Fig. 3e. When a hole is injected, the charge of the Fc-amm cation is increased from +1 to +2. Thus, it is more strongly attracted to PF_6^- anion and repelled from neighboring Fc-amm cations. The experimentally observed motion, schematically shown in Fig. 5a-b, corresponds to these electrostatic forces. Indeed, in the "excited phase", the Fc unit is a little closer to the PF_6^- anion and further away from the neighboring Fc-amm$^+$ cations.

A precise DFT calculation is difficult because of the very large unit cell, but we can estimate the order of magnitude of the electrostatic energy gain induced by the lateral motion. To this end, we consider a pair of Fc-amm ions modeled as point charges. Let their distance between two Fc-groups be R in the stable phase and $R' = R + \Delta R$ in the exited phase after hole injection. The injection of one hole increases the charge of one ion from +e to +2e, and thus, their Coulomb energy increases from $E_0(R) = k/R$ to $E_{ex}(R) = 2k/R$, where $k = e^2/4\pi\varepsilon_0 = 1.44$ eV nm, i.e. there is an energy rise of $\Delta E(R) = E_{ex}(R) - E_0(R) = k/R$. If the distance of the cations is $R' = R + \Delta R$, the energy rise is less; the relative energy change between the distances R and $R + \Delta R$ is $\Delta^2 E = \Delta E(R + \Delta R) - \Delta E(R) = -k\,\Delta R/[R\,(R + \Delta R)]$. For the estimated values of R = 1 nm, ΔR = 0.1 nm, we have $\Delta^2 E$ = -0.13 eV.

This means that the nearest neighbor pair of single- and double-charged Fc-amm ions can lower its electrostatic energy (with respect to that of the single-charged pair) by 0.13 eV when increasing its distance by 0.1 nm. If a hole is injected in each cation in the pair, the energy gain is 3 times larger, about 0.4 eV. These energy values are comparable to the adsorption energy cost (0.1 eV) due to the Fc shift (see Fig. 5b). This rough estimation shows that upon hole injection, the Fc lateral motion of about 0.1 nm may become energetically stable because the loss in adsorption energy is compensated by a gain in electrostatic energy.

In summary (Fig. 5c), the motion process could occur as follows: (1) hole injection, (2) oxidation: Fe^{2+} → Fe^{3+}, (3) Coulomb repulsive interaction → motion activation, (4) weakening of CH-π interaction, and finally (5) lateral sliding of Fc-amm.

4. Conclusions

Motion activation in molecular nanomachines, anchored in host-guest compounds employing the guest Fc-amm and the host BrCR molecules, synthesized in bulk solution, have undergone comprehensive exploration in recent decades. However, the electronic interaction from noble metals has led to the decomposition of Fc molecules, imposing constraints on the direct engagement of Fc-based compounds with metal electrodes.

In this investigation, we used a custom UHV-STM/STS setup operated at cryogenic temperatures. Utilizing the Cu(111) substrate effectively entrapped the guest Fc-amm within the host BrCR array at 300 K in UHV, as the Cu(111) surface activates the trapping capability of BrCR, a phenomenon that does not occur on the commonly employed Au substrate. This success can be attributed to the electronic decoupling and simultaneous trapping functionalities of the BrCR, averting the decomposition of the guest Fc-amm molecules. The regularity of Fc-amm is dictated by the intermolecular interactions between (1) Fc-amm and BrCR and (2) Fc-amm and Fc-amm, thereby dictating the alignment of Fc-amm along a specific direction or the formation of a densely packed ordered array, contingent upon the distance between individual Fc-amm molecules.

In conjunction with comprehensive STS electronic structure analysis, experimental evidence derived from STM topographic images identified the coexistence of face-on and edge-on Fc-amm on the BrCR array. Notably, only the edge-on Fc exhibited bias-dependent reversible structural variations when a hole was injected from the STM tip into the Fc HOMO. DFT calculations elucidated the sliding motion mechanism, wherein hole injection facilitated the oxidation from Fe^{2+} to Fe^{3+}, thereby enhancing the Coulombic repulsive interactions between molecules and resulting in lateral sliding motion. This hole-injection-induced lateral motion of Fc-amm is accompanied by a slight twisting of the Fc molecule, reminiscent of the well-known redox-induced internal rotation of ferrocene in bulk.

Thus, we have observed a novel, experimentally controlled molecular motion in a host-guest complex. This kind of stimulated, charge transfer-driven molecular motion is expected to play a crucial role in various biological, chemical, and physical phenomena, including photosynthesis, redox reactions, and molecular electronics.

Conflicts of interest

The authors declare no competing financial interest.

Author contributions

F.N. and T.K.Y. co-wrote the original manuscript, and all co-authors meticulously reviewed and corrected it. C.H.W., Y.H.C., and M.H. synthesized and evaluated the organic molecules. STM/STS measurements were conducted by F.N., R.N., and T.K.Y. DFT calculations were performed by P.K. X-ray photoemission spectroscopy measurements were carried out by F.N., T.H., Y.H., K.F., and S.K. T.K.Y. led the study.

Acknowledgments

This work was supported by JSPS KAKENHI Grant Numbers 17K19023, 23H02033, and 23H05461, the Murata Science Foundation, Shorai Foundation for Science and Technology, TEPCO Memorial Foundation, Cooperative Research by Institute for Molecular Science (IMS program 21-205), and Casio Science Foundation. We thank Prof. Dr. Eiichi Inami (Koch University of Technology) and Mr. Haruki Ishii for their technical support for the STS analysis.

References

(1) Rai, V.; Balzer, N.; Derenbach, G.; Holzer, C.; Mayor, M.; Wulfhekel, W.; Gerhard, L.; Valášek, M. Hot Luminescence from Single-Molecule Chromophores Electrically and Mechanically Self-Decoupled by Tripodal Scaffolds. *Nat. Commun.* **2023**, *14* (1), 8253. https://doi.org/10.1038/s41467-023-43948-y.

(2) Bauer, A.; Maier, M.; Schosser, W. M.; Diegel, J.; Paschke, F.; Dedkov, Y.; Pauly, F.; Winter, R. F.; Fonin, M. Tip-Induced Inversion of the Chirality of a Molecule's Adsorption Potential Probed by the Switching Directionality. *Adv. Mater.* **2020**, *32* (12), 1907390. https://doi.org/10.1002/adma.201907390.

(3) Mishra, P.; Hill, J. P.; Vijayaraghavan, S.; Rossom, W. V.; Yoshizawa, S.; Grisolia, M.; Echeverria, J.; Ono, T.; Ariga, K.; Nakayama, T.; Joachim, C.; Uchihashi, T. Current-Driven Supramolecular Motor with In Situ Surface Chiral Directionality Switching. *Nano Lett.* **2015**, *15* (7), 4793–4798. https://doi.org/10.1021/acs.nanolett.5b01908.

(4) Kay, E. R.; Leigh, D. A.; Zerbetto, F. Synthetic Molecular Motors and Mechanical Machines. *Angew. Chem. Int. Ed.* **2007**, *46* (1–2), 72–191. https://doi.org/10.1002/anie.200504313.

(5) Horie, M.; Wang, C.-H. Stimuli-Responsive Dynamic Pseudorotaxane Crystals. *Mater. Chem. Front.* **2019**, *3* (11), 2258–2269. https://doi.org/10.1039/C9QM00483A.

(6) Wang, C.-H.; Horie, M. Photo and Thermal Responsive Pseudorotaxane Crystals Comprising Ferrocene-Containing Ammonium Salts and Crown Ethers. *Mater. Today Chem.* **2022**, *24*, 100852. https://doi.org/10.1016/j.mtchem.2022.100852.

(7) Wang, C.-H.; Lin, Y.-C.; Bhunia, S.; Feng, Y.; Kundu, P.; Stern, C. L.; Chen, P.-L.; Stoddart, J. F.; Horie, M. Photosalience and Thermal Phase Transitions of Azobenzene- and Crown Ether-Based Complexes in Polymorphic Crystals. *J. Am. Chem. Soc.* **2023**, *145* (39), 21378–21386. https://doi.org/10.1021/jacs.3c06371.

(8) Chen, K.-J.; Tsai, Y.-C.; Suzaki, Y.; Osakada, K.; Miura, A.; Horie, M. Rapid and Reversible Photoinduced Switching of a Rotaxane Crystal. *Nat. Commun.* **2016**, *7* (1), 13321. https://doi.org/10.1038/ncomms13321.

(9) Cheng, S.-C.; Chen, K.-J.; Suzaki, Y.; Tsuchido, Y.; Kuo, T.-S.; Osakada, K.; Horie, M. Reversible Laser-Induced Bending of Pseudorotaxane Crystals. *J. Am. Chem. Soc.* **2018**, *140* (1), 90–93. https://doi.org/10.1021/jacs.7b10998.

(10) Cheng, S.-C.; Wang, C.-H.; Lin, Y.-C.; Tsuchido, Y.; Suzaki, Y.; Sei, Y.; Kuo, T.-S.; Horie, M. Photoinduced Mechanical Motions of Pseudorotaxane Crystals Composed of Azobenzene and Ferrocenyl Groups on an Axle and a Crown Ether Ring. *ACS Appl. Mater. Interfaces* **2020**, *12* (44), 50002–50010. https://doi.org/10.1021/acsami.0c15171.

(11) Wang, C. H.; Chen, K. J.; Wu, T. H.; Chang, H. K.; Tsuchido, Y.; Sei, Y.; Chen, P. L.; Horie, M. Ring Rotation of Ferrocene in Interlocked Molecules in Single Crystals. *Chem. Sci.* **2021**, *12* (11), 3871–3875. https://doi.org/10.1039/d0sc06876d.

(12) Hosokai, T.; Horie, M.; Aoki, T.; Nagamatsu, S.; Kera, S.; Okudaira, K. K.; Ueno, N. Change in Molecular Conformation of Dibenzo-Crown Ether Induced by Weak Molecule−Substrate Interaction. *J. Phys. Chem. C* **2008**, *112* (12), 4643–4648. https://doi.org/10.1021/jp710835b.

(13) Nemoto, R.; Krüger, P.; Putri Hartini, A. N.; Hosokai, T.; Horie, M.; Kera, S.; Yamada, T. K. Well-Ordered Monolayer Growth of Crown-Ether Ring Molecules on Cu(111) in Ultra-High Vacuum: An STM, UPS, and DFT Study. *J. Phys. Chem. C* **2019**, *123* (31), 18939–18950. https://doi.org/10.1021/acs.jpcc.9b03335.

(14) Yamada, T. K.; Nemoto, R.; Nishino, F.; Hosokai, T.; Wang, C.-H.; Horie, M.; Hasegawa, Y.; Kera, S.; Krüger, P. On-Surface Growth of Transition-Metal Cobalt Nanoclusters Using a 2D Crown-Ether Array. *J. Mater. Chem. C* **2024**, 10.1039.D3TC03339B. https://doi.org/10.1039/D3TC03339B.

(15) Yamada, T. K.; Nemoto, R.; Ishii, H.; Nishino, F.; Chang, Y.-H.; Wang, C.-H.; Krüger, P.; Horie, M. Designing 2D Stripe Winding Network through Crown-Ether Intermediate Ullmann Coupling on Cu(111) Surface. *Nanoscale Horiz.* **2024**, *9* (5), 718–730. https://doi.org/10.1039/D3NH00586K.

(16) Heinze, K.; Lang, H. Ferrocene—Beauty and Function. *Organometallics* **2013**, *32* (20), 5623–5625. https://doi.org/10.1021/om400962w.

(17) Ormaza, M.; Abufager, P.; Bachellier, N.; Robles, R.; Verot, M.; Le Bahers, T.; Bocquet, M.-L.; Lorente, N.; Limot, L. Assembly of Ferrocene Molecules on Metal Surfaces Revisited. *J. Phys. Chem. Lett.* **2015**, *6* (3), 395–400. https://doi.org/10.1021/jz5026118.

(18) Paul, A.; Borrelli, R.; Bouyanfif, H.; Gottis, S.; Sauvage, F. Tunable Redox Potential, Optical Properties, and Enhanced Stability of Modified Ferrocene-Based Complexes. *ACS Omega* **2019**, *4* (12), 14780–14789. https://doi.org/10.1021/acsomega.9b01341.

(19) Camarasa-Gómez, M.; Hernangómez-Pérez, D.; Inkpen, M. S.; Lovat, G.; Fung, E.-D.; Roy, X.; Venkataraman, L.; Evers, F. Mechanically Tunable Quantum Interference in Ferrocene-Based Single-Molecule Junctions. *Nano Lett.* **2020**, *20* (9), 6381–6386. https://doi.org/10.1021/acs.nanolett.0c01956.

(20) Berger, J.; Ondráček, M.; Stetsovych, O.; Malý, P.; Holý, P.; Rybáček, J.; Švec, M.; Stará, I. G.; Mančal, T.; Starý, I.; Jelínek, P. Quantum Dissipation Driven by Electron Transfer within a Single Molecule Investigated with Atomic Force Microscopy. *Nat. Commun.* **2020**, *11* (1), 1337. https://doi.org/10.1038/s41467-020-15054-w.

(21) Scottwell, S. Ø.; Crowley, J. D. Ferrocene-Containing Non-Interlocked Molecular Machines. *Chem. Commun.* **2016**, *52* (12), 2451–2464. https://doi.org/10.1039/C5CC09569G.

(22) Liu, R.; Ke, S.-H.; Baranger, H. U.; Yang, W. Organometallic Spintronics: Dicobaltocene Switch. *Nano Lett.* **2005**, *5* (10), 1959–1962. https://doi.org/10.1021/nl0513380.

(23) Zhou, L.; Yang, S.-W.; Ng, M.-F.; Sullivan, M. B.; Tan; Shen, L. One-Dimensional Iron−Cyclopentadienyl Sandwich Molecular Wire with Half Metallic, Negative Differential Resistance and High-Spin Filter Efficiency Properties. *J. Am. Chem. Soc.* **2008**, *130* (12), 4023–4027. https://doi.org/10.1021/ja7100246.

(24) Wang, L.; Cai, Z.; Wang, J.; Lu, J.; Luo, G.; Lai, L.; Zhou, J.; Qin, R.; Gao, Z.; Yu, D.; Li, G.; Mei, W. N.; Sanvito, S. Novel One-Dimensional Organometallic Half Metals: Vanadium-Cyclopentadienyl, Vanadium-Cyclopentadienyl-Benzene, and Vanadium-Anthracene Wires. *Nano Lett.* **2008**, *8* (11), 3640–3644. https://doi.org/10.1021/nl8016016.

(25) Shen, X.; Yi, Z.; Shen, Z.; Zhao, X.; Wu, J.; Hou, S.; Sanvito, S. The Spin Filter Effect of Iron-Cyclopentadienyl Multidecker Clusters: The Role of the Electrode Band Structure and the Coupling Strength. *Nanotechnology* **2009**, *20* (38), 385401. https://doi.org/10.1088/0957-4484/20/38/385401.

(26) Yang, J.-F.; Zhou, L.; Han, Q.; Wang, X.-F. Bias-Controlled Giant Magnetoresistance through Cyclopentadienyl–Iron Multidecker Molecules. *J. Phys. Chem. C* **2012**, *116* (37), 19996–20001. https://doi.org/10.1021/jp300465e.

(27) Welipitiya, D.; Green, A.; Woods, J. P.; Dowben, P. A.; Robertson, B. W.; Byun, D.; Zhang, J. Ultraviolet and Electron Radiation Induced Fragmentation of Adsorbed Ferrocene. *J. Appl. Phys.* **1996**, *79* (11), 8730–8734. https://doi.org/10.1063/1.362474.

(28) Waldfried, C.; Welipitiya, D.; Hutchings, C. W.; De Silva, H. S. V.; Gallup, G. A.; Dowben, P. A.; Pai, W. W.; Zhang, J.; Wendelken, J. F.; Boag, N. M. Preferential Bonding Orientations of Ferrocene on Surfaces. *J. Phys. Chem. B* **1997**, *101* (47), 9782–9789. https://doi.org/10.1021/jp972496l.

(29) Woodbridge, C. M.; Pugmire, D. L.; Johnson, R. C.; Boag, N. M.; Langell, M. A. HREELS and XPS Studies of Ferrocene on Ag(100). *J. Phys. Chem. B* **2000**, *104* (14), 3085–3093. https://doi.org/10.1021/jp993235+.

(30) Braun, K.-F.; Iancu, V.; Pertaya, N.; Rieder, K.-H.; Hla, S.-W. Decompositional Incommensurate Growth of Ferrocene Molecules on a Au(111) Surface. *Phys. Rev. Lett.* **2006**, *96* (24), 246102. https://doi.org/10.1103/PhysRevLett.96.246102.

(31) Dowben, P. A.; Waldfried, C.; Komesu, T.; Welipitiya, D.; McAvoy, T.; Vescovo, E. The Occupied and Unoccupied Electronic Structure of Adsorbed Ferrocene. *Chem. Phys. Lett.* **1998**, *283* (1–2), 44–50. https://doi.org/10.1016/S0009-2614(97)01316-X.

(32) Durston, P. J.; Palmer, R. E. Adsorption and Decomposition of Ferrocene on Graphite Studied by HREELS and STM. *Surf. Sci.* **1998**, *400* (1–3), 277–280. https://doi.org/10.1016/S0039-6028(97)00884-4.

(33) Tanaka, H.; Satake, A.; Taniguchi, M. Direct Observation of Distinctive Electronic States of Ferrocene Moieties in Ferrocene-Bridged Trisporphyrin on Au(111) Using Scanning Tunneling Microscopy/Spectroscopy. *Langmuir* **2021**, *37* (21), 6468–6474. https://doi.org/10.1021/acs.langmuir.1c00602.

(34) Santhini, V. M.; Stetsovych, O.; Ondráček, M.; Mendieta Moreno, J. I.; Mutombo, P.; Torre, B.; Švec, M.; Klívar, J.; Stará, I. G.; Vázquez, H.; Starý, I.; Jelínek, P. On-Surface Synthesis of Polyferrocenylene and Its Single-Chain Conformational and Electrical Transport Properties. *Adv. Funct. Mater.* **2021**, *31* (5), 2006391. https://doi.org/10.1002/adfm.202006391.

(35) Heinrich, B. W.; Limot, L.; Rastei, M. V.; Iacovita, C.; Bucher, J. P.; Djimbi, D. M.; Massobrio, C.; Boero, M. Dispersion and Localization of Electronic States at a Ferrocene/Cu(111) Interface. *Phys. Rev. Lett.* **2011**, *107* (21), 216801. https://doi.org/10.1103/PhysRevLett.107.216801.

(36) Nazriq, N. K. M.; Krüger, P.; Yamada, T. K. Carbon Monoxide Stripe Motion Driven by Correlated Lateral Hopping in a 1.4 × 1.4 Monolayer Phase on Cu(111). *J. Phys. Chem. Lett.* **2020**, *11* (5), 1753–1761. https://doi.org/10.1021/acs.jpclett.9b03645.

(37) Nazriq, N. K. M.; Minamitani, E.; Yamada, T. K. CO-Tip Manipulation Using Repulsive Interactions. *Nanotechnology* **2018**, *29* (49), 495701. https://doi.org/10.1088/1361-6528/aae0df.

(38) Ayani, C. G.; Calleja, F.; Ibarburu, I. M.; Casado Aguilar, P.; Nazriq, N. K. M.; Yamada, T. K.; Garnica, M.; Vázquez De Parga, A. L.; Miranda, R. Switchable Molecular Functionalization of an STM Tip: From a Yu–Shiba–Rusinov Tip to a Kondo Tip. *Nanoscale* **2022**, *14* (40), 15111–15118. https://doi.org/10.1039/D1NR08227B.

(39) Yamaguchi, T.; Inami, E.; Goto, Y.; Sakai, Y.; Sasaki, S.; Ohno, T.; Yamada, T. K. Fabrication of Tungsten Tip Probes within 3 s by Using Flame Etching. *Rev. Sci. Instrum.* **2019**, *90* (6), 063701. https://doi.org/10.1063/1.5085251.

(40) Goto, Y.; Suizu, R.; Noguchi, Y.; Yamada, T. K. Oxidative Vaporization Etching for Molybdenum Tip Formation in Air. *Appl. Surf. Sci.* **2021**, *542*, 148642. https://doi.org/10.1016/j.apsusc.2020.148642.

(41) Yamada, T. K.; Abe, T.; Nazriq, N. M. K.; Irisawa, T. Electron-Bombarded 〈110〉-Oriented Tungsten Tips for Stable Tunneling Electron Emission. *Rev. Sci. Instrum.* **2016**, *87* (3), 033703. https://doi.org/10.1063/1.4943074.

(42) Schmaus, S.; Bagrets, A.; Nahas, Y.; Yamada, T. K.; Bork, A.; Bowen, M.; Beaurepaire, E.; Evers, F.; Wulfhekel, W. Giant Magnetoresistance through a Single Molecule. *Nat. Nanotechnol.* **2011**, *6* (3), 185–189. https://doi.org/10.1038/nnano.2011.11.

(43) Gerhard, L.; Yamada, T. K.; Balashov, T.; Takács, A. F.; Wesselink, R. J. H.; Däne, M.; Fechner, M.; Ostanin, S.; Ernst, A.; Mertig, I.; Wulfhekel, W. Magnetoelectric Coupling at Metal Surfaces. *Nat. Nanotechnol.* **2010**, *5* (11), 792–797. https://doi.org/10.1038/nnano.2010.214.

(44) Inami, E.; Yamaguchi, M.; Yamaguchi, T.; Shimasaki, M.; Yamada, T. K. Controlled Deposition Number of Organic Molecules Using Quartz Crystal Microbalance Evaluated by Scanning Tunneling Microscopy Single-Molecule-Counting. *Anal. Chem.* **2018**, *90* (15), 8954–8959. https://doi.org/10.1021/acs.analchem.8b01118.

(45) Ukraintsev, V. A. Data Evaluation Technique for Electron-Tunneling Spectroscopy. *Phys. Rev. B* **1996**, *53* (16), 11176–11185. https://doi.org/10.1103/PhysRevB.53.11176.

(46) Yamagishi, Y.; Nakashima, S.; Oiso, K.; Yamada, T. K. Recovery of Nanomolecular Electronic States from Tunneling Spectroscopy: LDOS of Low-Dimensional Phthalocyanine Molecular Structures on Cu(111). *Nanotechnology* **2013**, *24* (39), 395704. https://doi.org/10.1088/0957-4484/24/39/395704.

(47) Horcas, I.; Fernández, R.; Gómez-Rodríguez, J. M.; Colchero, J.; Gómez-Herrero, J.; Baro, A. M. WSXM : A Software for Scanning Probe Microscopy and a Tool for Nanotechnology. *Rev. Sci. Instrum.* **2007**, *78* (1), 013705. https://doi.org/10.1063/1.2432410.

(48) Grimme, S.; Antony, J.; Ehrlich, S.; Krieg, H. A Consistent and Accurate *Ab Initio* Parametrization of Density Functional Dispersion Correction (DFT-D) for the 94 Elements H-Pu. *J. Chem. Phys.* **2010**, *132* (15), 154104. https://doi.org/10.1063/1.3382344.

(49) Kresse, G.; Furthmüller, J. Efficient Iterative Schemes for *Ab Initio* Total-Energy Calculations Using a Plane-Wave Basis Set. *Phys. Rev. B* **1996**, *54* (16), 11169–11186. https://doi.org/10.1103/PhysRevB.54.11169.

(50) Kresse, G.; Joubert, D. From Ultrasoft Pseudopotentials to the Projector Augmented-Wave Method. *Phys. Rev. B* **1999**, *59* (3), 1758–1775. https://doi.org/10.1103/PhysRevB.59.1758.

(51) Teyssandier, J.; Feyter, S. D.; Mali, K. S. Host–Guest Chemistry in Two-Dimensional Supramolecular Networks. *Chem. Commun.* **2016**, *52* (77), 11465–11487. https://doi.org/10.1039/C6CC05256H.

(52) Nemoto, R.; Krüger, P.; Hosokai, T.; Horie, M.; Kera, S.; Yamada, T. K. Room-Temperature Deposition of Cobalt Monolayer on (7×4) Crown-Ether Ring Molecular Array: Ultra-High Vacuum STM and UPS Study. *Vac. Surf. Sci.* **2020**, *63* (9), 465–469. https://doi.org/10.1380/vss.63.465.

(53) Duhm, S.; Gerlach, A.; Salzmann, I.; Bröker, B.; Johnson, R. L.; Schreiber, F.; Koch, N. PTCDA on Au(111), Ag(111) and Cu(111): Correlation of Interface Charge Transfer to Bonding Distance. *Org. Electron.* **2008**, *9* (1), 111–118. https://doi.org/10.1016/j.orgel.2007.10.004.

(54) Romaner, L.; Nabok, D.; Puschnig, P.; Zojer, E.; Ambrosch-Draxl, C. Theoretical Study of PTCDA Adsorbed on the Coinage Metal Surfaces, Ag(111), Au(111) and Cu(111). *New J. Phys.* **2009**, *11* (5), 053010. https://doi.org/10.1088/1367-2630/11/5/053010.

(55) Heimel, G.; Duhm, S.; Salzmann, I.; Gerlach, A.; Strozecka, A.; Niederhausen, J.; Bürker, C.; Hosokai, T.; Fernandez-Torrente, I.; Schulze, G.; Winkler, S.; Wilke, A.; Schlesinger, R.; Frisch, J.; Bröker, B.; Vollmer, A.; Detlefs, B.; Pflaum, J.; Kera, S.; Franke, K. J.; Ueno, N.; Pascual, J. I.; Schreiber, F.; Koch, N. Charged and Metallic Molecular Monolayers through Surface-Induced Aromatic Stabilization. *Nat. Chem.* **2013**, *5* (3), 187–194. https://doi.org/10.1038/nchem.1572.

(56) Nazriq, N. K. M.; Krüger, P.; Yamada, T. K. Improving MgO/Fe Insulator-Metal Interface Structure through Oxygen-Precoating of Fe(0 0 1). *Appl. Surf. Sci.* **2023**, *618*, 156628. https://doi.org/10.1016/j.apsusc.2023.156628.

Figures / Figure captions

Figure 1

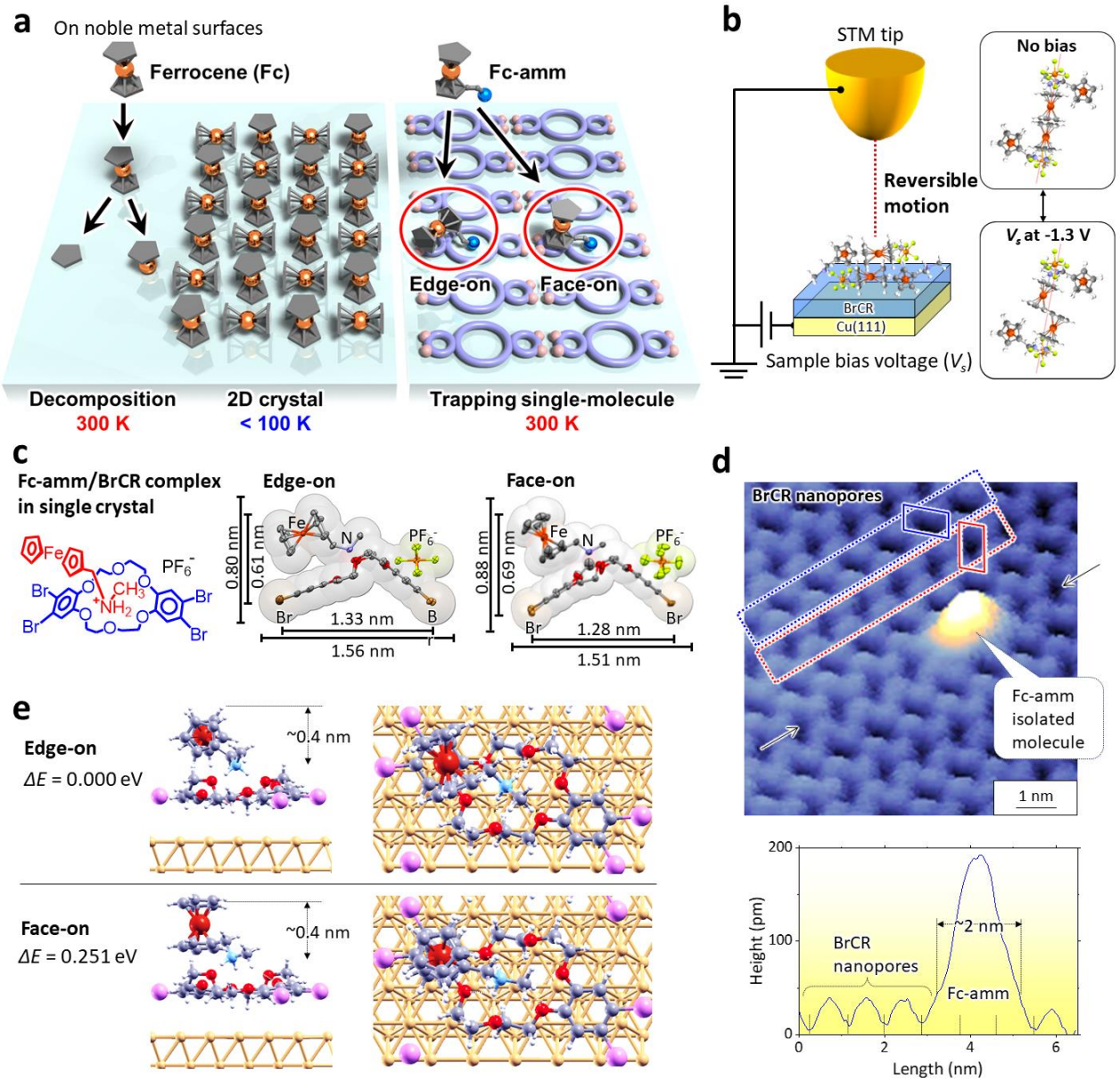

Figure 1. **Fc-amm on BrCR/Cu(111) at 300 K in UHV**. (a) Adsorption models of ferrocene (Fc) on noble metal surfaces in UHV in three cases: from left to right, when the substrate temperature at 300 K, below 100 K, and 300 K but with the BrCR precoating investigated in this study. (b) Model of the STM junction and the bias-dependent internal motion of the Fc-amm array on BrCR/Cu(111). (c) Molecular structures of the host BrCR and the guest Fc-amm complexes overlaying ORTEP (50% probability) and the space fill model. Hydrogen atoms were omitted for clarity. (d) STM topographic image in a 3D view mode obtained on the BrCR array on Cu(111) after depositing 0.1 monolayers (MLs) Fc-amm (8 nm × 8 nm, V_s = 1.8 V, I_t = 60 pA at 78 K). The lower panel denotes the height profile between two arrows. (e) The two most stable structures of a single Fc-amm molecule adsorbed on 1 ML BrCR/Cu(111) as obtained by DFT calculations (upper panel: edge-on, lower panel: face-on). ΔE denotes the energy difference with respect to the most energetically stable configuration (edge-on). Several other conformations have been found, but they are at least 0.7 eV higher in energy. (Supplementary, Fig. S14).

Figure 2

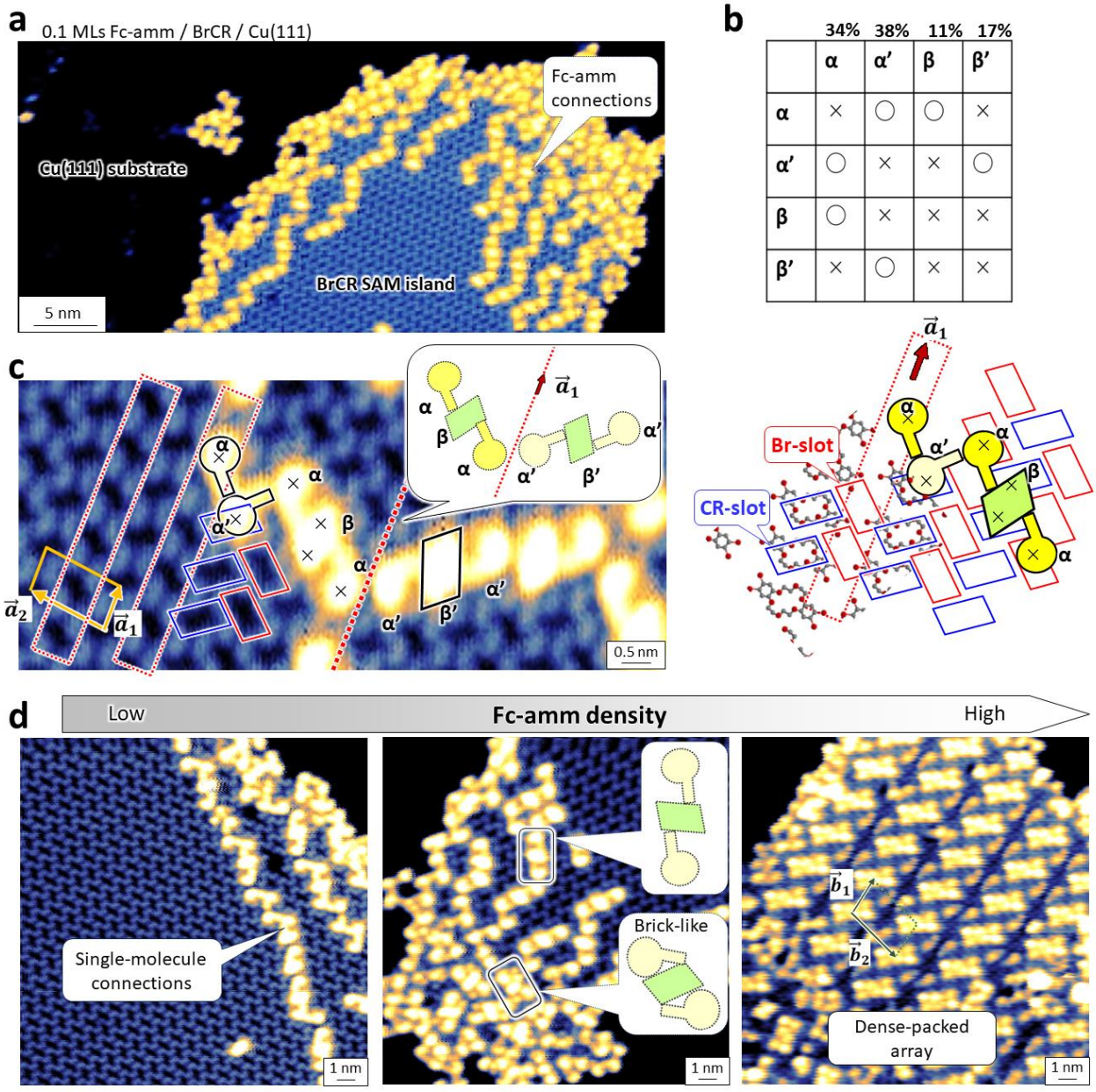

Figure 2. **Fc-amm ordered array on BrCR**. (a) STM topographic image (50 nm × 23 nm) obtained on the 0.8 MLs BrCR film prepared on the Cu (111) substrate after depositing 0.1 monolayers (MLs) Fc-amm at 300 K in UHV, which formed single-molecule connections (V_s = 1.8 V, I_t = 60 pA at 78 K). (b) Connection rules of α, β, α', and β' molecules. Symbols ○ and × denote experimentally observed or not. (c) Enlarged STM image (10 nm × 5 nm) obtained on the same surface as (a). Yellow arrows denote the BrCR molecular unit cell ($\boldsymbol{a_1}$ and $\boldsymbol{a_2}$). Fc-amm molecules follow the reflection symmetric blue and red slots in the BrCR nanoporous film. Dotted boxes denote the slot row. Each of the slots aligns alternatively. The right panel denotes the corresponding model. Type α, α', β and β' Fc-amm molecules and α-β-α and α'-β'-α' connections are shown. (d) STM topographic images (20 nm × 20 nm) obtained on the 0.8 MLs BrCR film prepared on the Cu (111) substrate after depositing 0.1, 0.2, and 0.3 MLs Fc-amm at 300 K in UHV, which formed single-molecule connections and brick-like dense-packed array, respectively (from left to right: V_s = 1.8 V, I_t = 60 pA; V_s = 1.2 V, I_t = 10 pA; V_s = -2.5 V, I_t = 11 pA at 78 K). Arrows denote the unit vectors ($\boldsymbol{b_1}$ and $\boldsymbol{b_2}$).

Figure 3

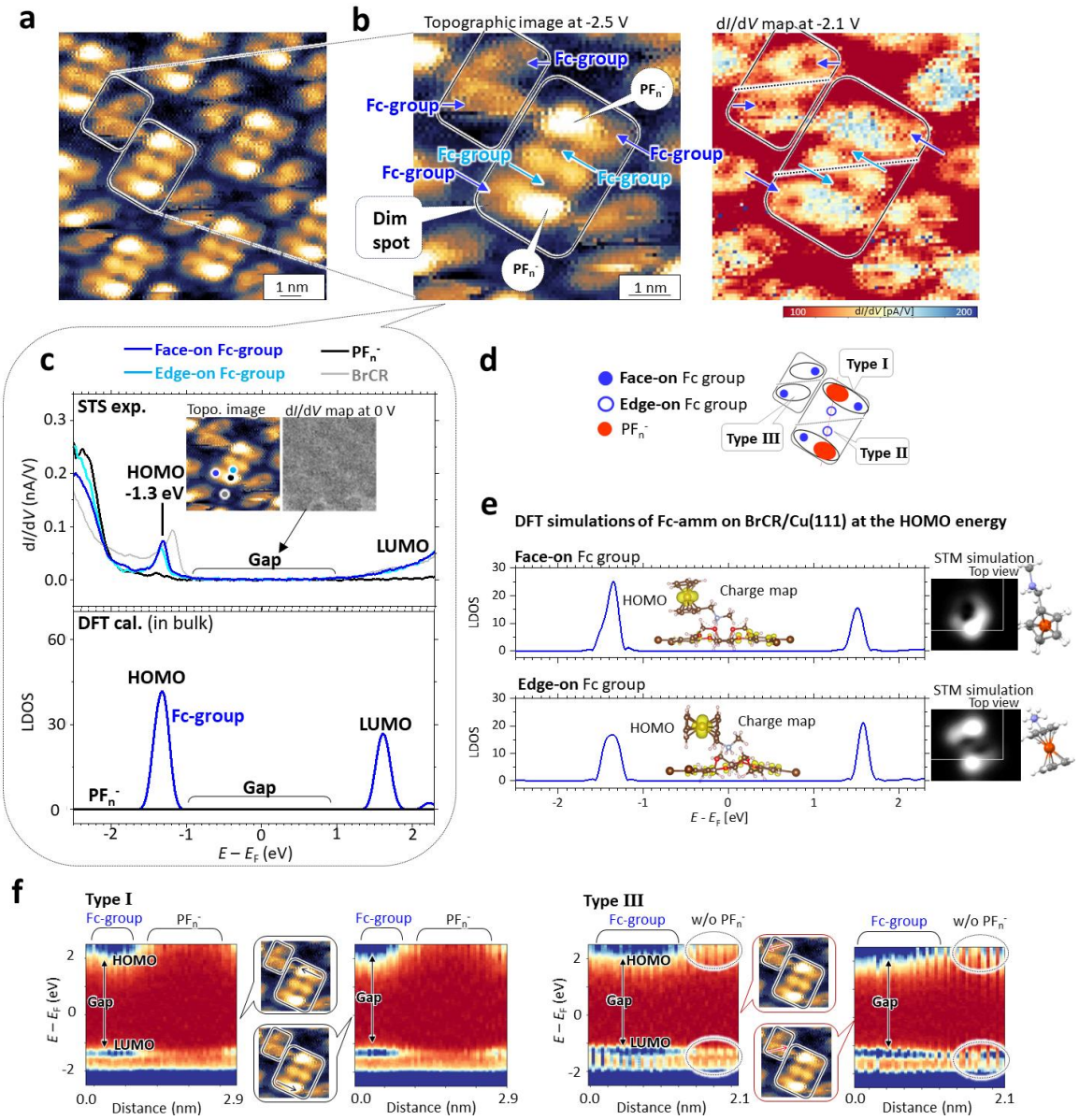

Figure 3. **Electronic structures of Fc-amm on BrCR**. (a) STM topographic image (13 nm × 13 nm, V_s = -2.5 V, I_t = 100 pA, 4.6 K) of the Fc-amm array. White boxes denote two kinds of ordered assembles. (b) Enlarged STM topographic image (6.5 nm × 6.5 nm) (left panel) and the simultaneously obtained STS dI/dV map at -2.1 V (right panel), which intensity is proportional to the sample LDOS. Fc-group and PF_n^- ligand denote the ferrocene group and side ligand positions. In the dI/dV map, a bright bot, including the off-centred dark dim, indicates the face-on Fc-group position. (c) Experimentally obtained dI/dV curves at blue, red, green, and grey positions, where the former two spectra show identical LDOS peaks, the third one shows no peaks around the Fermi energy, and the last one shows the BrCR LDOS. Lower panel: LDOS of the Fc-amm/BrCR bulk crystal obtained by the DFT calculation. (d) Three types: I, II, and III of Fc-amm compounds were experimentally found. Type I and III Fc-amm complexes could consist of the face-on Fc-group with and without PF_n^- ligand. Type II Fc-amm complex could consist of the edge-on Fc-group, possibly without PF_n^- ligand. (e) DFT simulation results of the LDOS for face-on and edge-on Fc-amm adsorbed on BrCR/Cu(111). (f) 3D dI/dV maps obtained along four arrows (see indexes in maps) in the type I and III Fc-amm compounds; x, y, and z axes denote distance (nm), energy: E-E_F (eV), and dI/dV intensity, respectively.

Figure 4

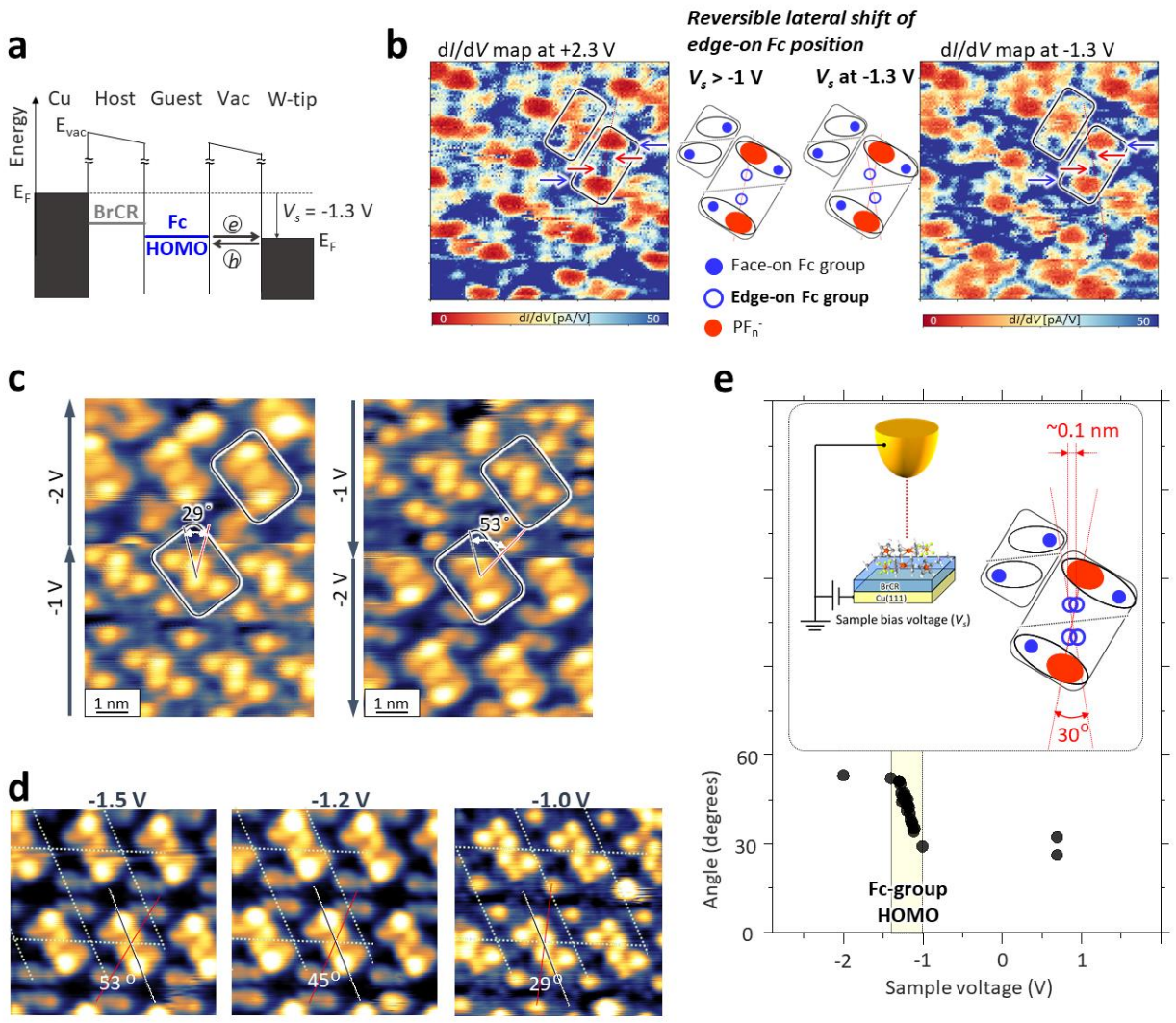

Figure 4. **Motion activation in the Fc-amm array**. (a) Energy diagrams of the tunneling process through the double barrier system in the Fc-amm/BrCR/Cu(111), representing the hole injection into the Fc-group's HOMO at negative bias application. (b) d*I*/d*V* maps at -2.1 V and -1.3 V (I_t = 100 pA, 4.6 K). Arrows denote the Fc-group positions: blue and red dots denote face-on and edge-on Fc-group positions. Green dots represent the PF_n^- ligand position. (c) STM topographic images scanned from (left panel) bottom to top and (right panel) from top to down at -1 V and -2 V (I_t = 10 pA). Angles between two lines varied at different bias applications. (d) A series of Fc-amm STM topographic images were obtained in the same area at different bias voltages: -1.5, -1.2, and -1.0 V. (e) Angle variations as a function of the sample bias voltage, indicating the reversible motion of the edge-on Fc-amm compounds occurs in the vicinity of the Fc-group's HOMO position.

Figure CH-π interaction

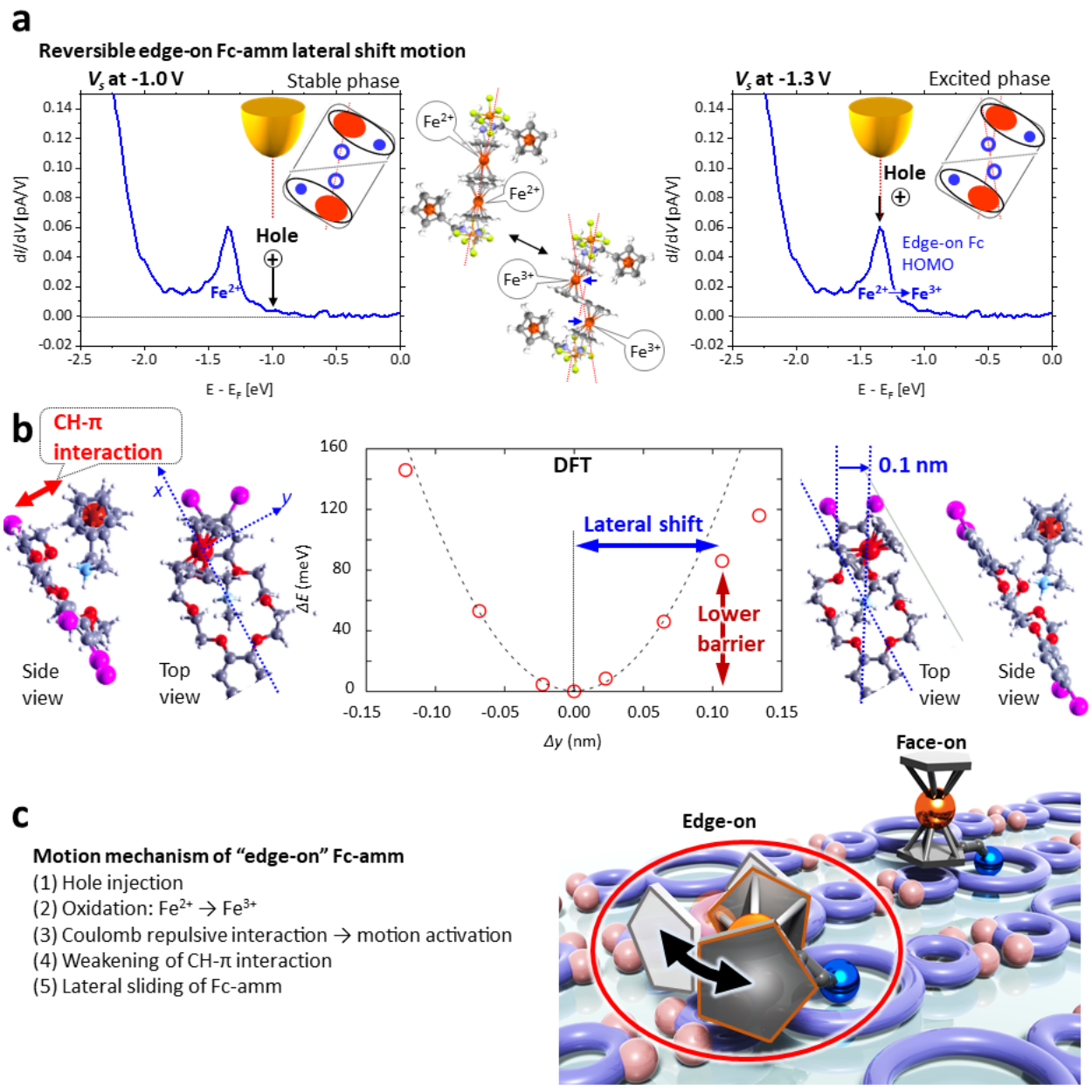

Figure 5. **Reversible motion mechanism of Fc-amm on BrCR**. (a) Left panel: no motion at a sample bias (V_s) of -1.0 V. Right panel: experimentally obtained reversible lateral position shifts for edge-on Fc-amm molecules at V_s = -1.3 V. (b) DFT-calculated energy diagram as a function of the lateral shift along the *y*-axis (Δy), indicating that only a right-hand side shift can occur due to the asymmetry of the energy barrier. The red circles represent the calculated values, while the dashed line references the parabolic curve. The DFT simulation suggests that the change in CH-π interaction related to the lateral motion. Due to a single energy minimum, the lateral shift returns to the original position when the hole injection stops. (c) Motion mechanism processes of the "edge-on" Fc-amm and (right panel) proposed model depicting the internal motions of the Fc-amm compound confined within the BrCR array.